Active control of sound transmission using a hybrid/blind decentralized control approach

Ming Yuan, Jinhao Qiu, Hongli Ji, Weiyinuo Zhou, Roger Ohayon

To cite this version:

Ming Yuan, Jinhao Qiu, Hongli Ji, Weiyinuo Zhou, Roger Ohayon. Active control of sound transmission using a hybrid/blind decentralized control approach. Journal of Vibration and Control, 2015, 21 (13), pp.2661-2684. 10.1177/1077546313514758 . hal-03177143

Active control of sound transmission using a hybrid/blind decentralized control approach

Ming Yuan[1,2], Jinhao Qiu[1], Hongli Ji[1], Weiyinuo Zhou[1] and
Roger Ohayon[2]

This paper presents a theoretical and experimental analysis of broadband sound transmission control of an aluminum panel in the frequency range between 30 Hz and 1 kHz. Based on the analysis of characteristics of sensor-actuator pairs, piezoelectric patches bonded on the structure are used as actuators, and collocated accelerometers are used as sensors. Then a hybrid decentralized control law is derived, which has a broad control band and puts more control authority on the most sound radiation effective mode. This control law comprises two parts: one is the direct velocity feedback controller, and the other one, relatively new, is called the negative acceleration feedback (NAF) controller. The control architecture is decentralized, which means each controller works independently. Due to the second-order dynamic property of the NAF controller and the fact that the structure's frequencies may shift, the Hilbert-Huang method is used for quick and automatic identification of the natural frequency. Finally, open loop and closed loop experiments are presented to support the theoretical analysis. The active control results demonstrate that the panel's vibration level can be suppressed by 16.7 dB and the broadband sound pressure level could be lowered by more than 7 dB.

Keywords
Collocated configuration, decentralized active control, hybrid control, smart structure, sound transmission

1. Introduction

Noise transmission control has had a wide range of applications in recent years, such as civil aviation and transportation. The high levels of interior noise generated by engines and turbulent boundary layer have serious negative influences on communication and people's health. One way to tackle the stochastic noise inside a vehicle's cabin is to reduce the sound transmission to the zone of interest (Elliott, 1994). However, these panels' sound isolation performance is poor, as they suffer from vibrations, which makes the outside noise transmission into the cabin easier. This problem is even more severe at low frequencies, where it has been widely accepted that passive control is not effective due to added volume and mass. Fortunately, in this band, active control of sound transmission is much more effective than the passive approach, and a lot of researchers have made much effort in recent years to make such a control system more practical (Hansen, 2003; Yuan et al., 2012). Generally, these active solutions focus on the reduction of the structure's sound radiation through effective change of the dynamic behavior of the structure. This approach is commonly called active structural acoustic control (ASAC), which was first proposed in the 1990s (Fuller et al., 1996).

Among different approaches of ASAC, the feedforward control has been carried out in some large projects, such as propeller and helicopter noise control (Grewal et al., 2000; Chen et al., 2004). A good reference signal is needed for effective control. As the control performance is largely influenced by the correlation between the

---

[1]State Key Laboratory of Mechanics and Control of Mechanical Structures, College of Aerospace Engineering, Nanjing University of Aeronautics and Astronautics, Nanjing, Jiangsu, China
[2]Conservatoire National des Arts et Métiers, Structural Mechanics and Coupled Systems Laboratory, Paris, France

Received: 11 December 2012; accepted: 27 October 2013

Corresponding author:
Jinhao Qiu, State Key Laboratory of Mechanics and Control of Mechanical Structures, Nanjing University of Aeronautics & Astronautics, #29 Yudao Street, Nanjing 210016, China.
Email: qiu@nuaa.edu.cn

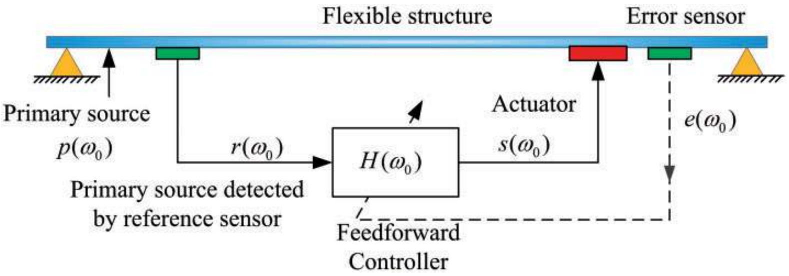

Figure 1. Schematic diagram of feedforward active controller.

disturbance and the reference signal, the reference signal is usually a tachometer or accelerometer signal which should have strong correlation with the disturbance noise. However, in most cases, the reference signal is poor or unavailable. For instance, when an aircraft flies, turbulent boundary layer noise will impinge persistently on the fuselages and generates many uncorrelated sources, which makes it difficult to find a single reference signal that is coherent with the excitation. Even if a correlation source is available, the control performance will downgrade sharply due to poor correlation quality (Elliott, 1994). Thus, it is imperative to use feedback control to improve the structure's sound isolation performance in the low-frequency band.

The general structures (Fahy and Gardonio, 2007) of feedforward and feedback control of the sound transmission system are shown in Figures 1 and 2 respectively.

With respect to feedback control, independent modal space control (Meirovitch, 1990) is a classical approach for low frequency vibration suppression. Other control laws and sensing strategies have been optimized for the audio frequency band, such as volume velocity estimation (Johnson and Elliott, 1995), radiation mode expansion (Gibbs et al., 2000), optimal control (Strassberger and Waller, 2000), predictive control (Dozio and Ghiringhelli, 2008), H infinity control (Choi, 2006), boundary control (Jemai et al., 2002) and neural network fitting (Ji et al., 2009). Generally, all references above could be summarized as centralized control, which usually needs precise system identification and modeling for effective broadband disturbance rejection. Concerning active sound transmission control, which covers audio frequency in broadband, the orders of the designed controller may be as high as the hundreds when the modal density is high. This requires high performance control hardware and thus increases the system's cost. In addition, instability may occur if one of the channels fails due to numerical computation errors or sensor/actuator wears.

Therefore, in recent years, active control of noise and vibration system with one multiple input-multiple output (MIMO) controller that has a large number of sensors and actuators has been evolved into system with multiple decentralized single input-single output (SISO) controllers. Each control loop is equipped with a pair of collocated sensor/actuators, which makes the system simple and robust (Gardonio, 2002). For instance, Engels et al. (2006) demonstrated that multiple decentralized control loops have almost the same control performance as the centralized controller. Gardonio et al. (2004a,b,c) used 16 decentralized control loops to actively control the sound transmission with direct velocity feedback control (DVF). The DVF control law can be used for broadband structure damping. Besides DVF, there are many other decentralized control approaches, such as positive position feedback control (PPF) (Fanson and Caughey, 1990; Friswell and Inman, 1999; Wang and Inman, 2011), and integral resonant control (IRC) (Aphale et al., 2007), etc. These control laws alleviated the needs of a structure's information compared with centralized control methods.

Hence, decentralized feedback control architecture should be considered. However, for the audio frequency feedback control, the DVF control law's performance is usually limited, because its control authorities are distributed on each mode. Therefore, it is interesting to develop some hybrid control law which is not only broadband but also more effective than DVF. Besides, the robust performance of the hybrid control law should not be degraded and the expression should still be kept simple for easy implementation.

To solve the problem above, the present work investigates thoroughly a hybrid decentralized feedback control method. In Section 2, the dynamic responses of a structure's sound and vibration characteristics are formulated. In Section 3, in order to achieve maximum active damping, compact sensor and actuator selections are discussed. Based on the analyses of previous sections, in Section 4, a hybrid control law which combines the features of narrow band control and broadband control is proposed. In Section 5, the Hilbert-Huang method is proposed to update the

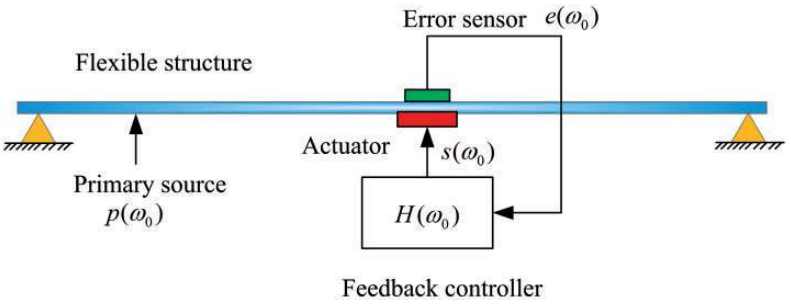

Figure 2. Schematic diagram of feedback active controller.

control law's parameters. In Section 6, experimental test structures are designed and the acoustic location's influence on the structure's response is discussed. Open loop analyses are also carried out for implementation and stability discussions. Closed loop experiment results, both structurally and acoustically, are discussed in Section 7. Finally, conclusions are given in Section 8.

2. Structural modeling and sound radiation theory

2.1. Structural modeling

As the interested control domain's modal density is not high, the modal solution is applicable to compute the modes of the system (Ohayon and Soize, 1998). The general equation of the motion of structure can be expressed as a multiple-degrees-of-freedom (m-d.f.) discrete parameter system. When the active force of piezoelectric exerts upon the structure, the equation of the motion of such an m-d.f. system can be written as:

$$\mathbf{M}\ddot{\mathbf{w}} + \mathbf{C}\dot{\mathbf{w}} + \mathbf{K}\mathbf{w} = \mathbf{F} + \alpha \cdot \mathbf{V} \tag{1}$$

where

- $\mathbf{M}$, $\mathbf{C}$, $\mathbf{K}$ are $(n \times n)$ mass, damping and stiffness matrix respectively, $\mathbf{C}$ is considered as Rayleigh damping, which has the form $\mathbf{C} = \alpha\mathbf{M} + \beta\mathbf{K}$,
- $\mathbf{w}$ is the $(n \times 1)$ displacement vector, $\mathbf{F}$ is the primary disturbance force vector,
- α is the converting coefficient between the control voltage and the output force,
- $\mathbf{V}$ is the control voltage vector exerting on the piezoelectric patches,
- $\alpha \cdot \mathbf{V}$ is the secondary control force.

Defining $\mathbf{w} = \mathbf{\Phi}\mathbf{x}(t)$, and substituting it into equation (1), yields:

$$\mathbf{M\Phi}\ddot{\mathbf{x}} + \mathbf{C\Phi}\dot{\mathbf{x}} + \mathbf{K\Phi}\mathbf{x} = \mathbf{F} + \alpha \cdot \mathbf{V} \tag{2}$$

where $\mathbf{\Phi} = [\phi_1\ \phi_2\ \ \ldots\ \ \phi_N]$ is the modal matrix whose columns are the respective normal modes and $\mathbf{x}$ is the modal vector.

If the natural modes are normalized, which means $\mathbf{\Phi}^T\mathbf{M}\mathbf{\Phi} = \mathbf{I}$, equation (2) can be further simplified into equation (3):

$$\mathbf{I}\ddot{\mathbf{x}} + \mathbf{C}\dot{\mathbf{x}} + \boldsymbol{\omega}^2\mathbf{x} = \mathbf{f} \tag{3}$$

where

- $\mathbf{C} = \mathbf{\Phi}^T\mathbf{C}\mathbf{\Phi}_N = diag(2\xi_r\omega_r M_r)$ is the diagonal modal damping matrix,
- $\boldsymbol{\omega} = diag(\omega_1^2, \omega_2^2, \ldots, \omega_N^2)$ is the diagonal modal frequency matrix,
- $\mathbf{f} = \mathbf{\Phi}^{\mathbf{T}} \cdot (\mathbf{F} + \alpha \cdot \mathbf{V})$ is the modal force vector.

After the modal transformation, the coupled m-d.f. dynamic system can now be represented by N degrees of an independent single-degree-of-freedom (s-d.f.) vibrating system, and controller designs can be simplified by the decoupling, which is shown in Figure 3.

2.2. Characteristics of sound radiation problem

A geometric schematic diagram of a baffled rectangular panel is shown in Figure 4:

For effective controller design, in order to exert enough control authority, we need to identify which mode radiates the most. The sound radiation of the panel and the transverse vibration velocity can be represented by the Rayleigh integral (St Pierre, 1998):

$$p(R,\theta,\phi) = \frac{i\omega\rho e^{ikR}}{2\pi R} \times \int_{-L_x}^{L_x}\int_{-L_y}^{L_y} \dot{w}(x_0,y_0)e^{-ik\sin\theta(x_0\cos\phi + y_0\sin\phi)}\mathrm{d}x_0\mathrm{d}y_0 \tag{4}$$

where

- L_x, L_y, θ, ϕ and R are shown in Figure 4,
- $p(R,\theta,\phi)$ is the far-field sound pressure,

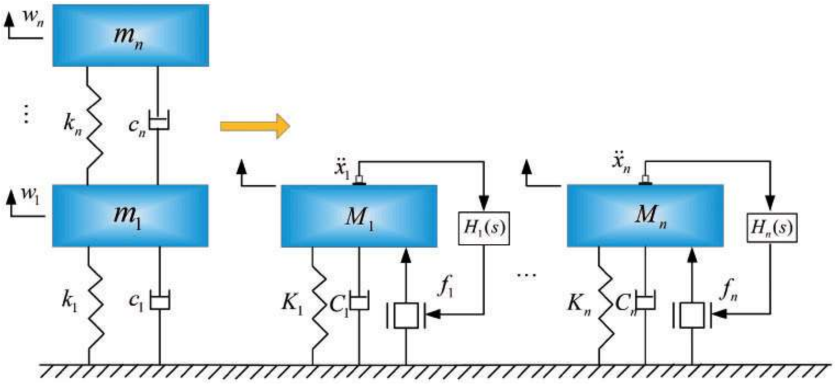

Figure 3. Multi-degree-of-freedom dynamic system decoupling and controller design.

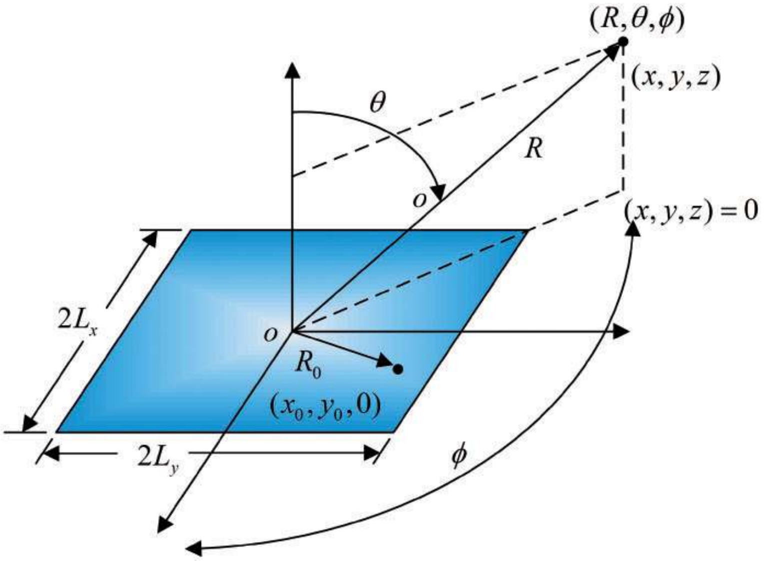

Figure 4. Schematic diagram of sound radiation of an infinite baffled panel.

- k is the acoustic wavenumber,
- ω is the angular frequency,
- ρ is the density of the acoustic medium,
- $\dot{w}(x_0, y_0)$ is the vibration velocity located at (x_0, y_0).

Deduced from equation (4), the radiation efficiency can be defined as (Wallace, 1972):

1. When m, n are both odd integers,

$$S_{mn} \approx \frac{32k^2ab}{m^2n^2\pi^5}\left\{1-\frac{k^2ab}{12}\left[\left(1-\frac{8}{(m\pi)^2}\right)\frac{a}{b}+\left(1-\frac{8}{(n\pi)^2}\right)\frac{b}{a}\right]\right\}, \quad ka, kb \ll 1 \tag{5}$$

2. When m is odd integer and n is even integer,

$$S_{mn} \approx \frac{8k^4ab^3}{3m^2n^2\pi^5}\left\{1-\frac{k^2ab}{20}\left[\left(1-\frac{8}{(m\pi)^2}\right)\frac{a}{b}+\left(1-\frac{24}{(n\pi)^2}\right)\frac{b}{a}\right]\right\}, \quad ka, kb \ll 1 \tag{6}$$

3. When m, n are both even integers,

$$S_{mn} \approx \frac{2k^6a^3b^3}{15m^2n^2\pi^5}\left\{1-\frac{5k^2ab}{64}\left[\left(1-\frac{24}{(m\pi)^2}\right)\frac{a}{b} + \left(1-\frac{24}{(n\pi)^2}\right)\frac{b}{a}\right]\right\}, \quad ka, kb \ll 1 \tag{7}$$

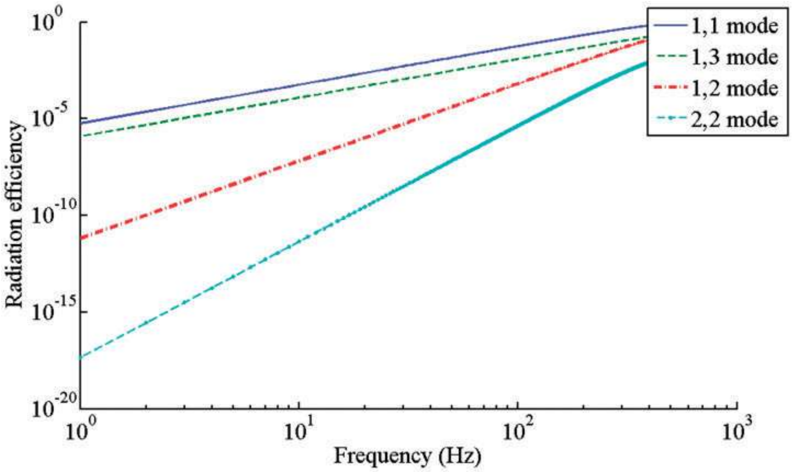

Figure 5. Radiation efficiencies of the panel's selected lower modes.

where

- $a = 2L_x$, $b = 2L_y$,
- k is the acoustic wavenumber.

Such results are obtained using a simple support boundary. For the clamped boundary, the mode's radiation efficiency is almost the same. The boundary conditions mainly influence the natural frequencies and the mode shapes, but have little influence on the mode's radiation efficiency (Berry et al., 1990). With regard to a square vibrating panel (see its parameters in Section 6), the corresponding radiation efficiencies of several low frequency modes are plotted in Figure 5.

It can be seen from this figure that the odd-odd mode's radiation efficiency is much larger than that of the odd-even and even-even vibration modes in the low frequencies. The 1,1 vibration mode radiates the most because it radiates like a monopole and suffers the least cancellation of radiation. Meanwhile, as a global vibration mode, it needs the most control effort.

3. Sensor-actuator selection for collocated feedback control

3.1. The pole-zero spacing influence on feedback control performance

Collocated control is notable for the property of pole-zero interlacing (Preumont, 2011). It also indicates the phase response of the collocated transfer function varying within a range of 180 degrees. The generalized form is given in equation (8).

$$G(s) = G_0 \frac{\prod \left(s^2 + 2\xi_n s\omega_{nz} + \omega_{nz}^2\right)}{\prod \left(s^2 + 2\xi_m s\omega_{mp} + \omega_{mp}^2\right)} \tag{8}$$

An example to represent such a collocated transfer function above is given in equation (9), and its corresponding Bode plot is shown in Figure 6.

$$\begin{aligned} G(s) = {} & \frac{s^2 + 2 * 0.01 * 125.6s + 29500}{s^2 + 2 * 0.01 * 125.6s + 15775} \\ & \times \frac{s^2 + 2 * 0.01 * 314s + 105000}{s^2 + 2 * 0.01 * 314s + 98596} \\ & \times \frac{s^2 + 2 * 0.01 * 439.6s + 201000}{s^2 + 2 * 0.01 * 439.6s + 193248} \end{aligned} \tag{9}$$

If DVF control acts on this system, the root locus plot of the simulated system is shown in Figure 7.

As shown in Figure 6 and Figure 7, the zero-pole spacing is important to achieve the maximum damping by the active controller. If the pole-zero distance is very small, it suffers pole-zero cancellation and there are only small peaks on the magnitude response plot and little dips on the phase response plot. The corresponding root locus of such a system varies by only a small angle in the left half plane, which indicates poor active damping performance. For these reasons, in order to get satisfying control results, it is very important to select a proper sensor-actuator with enough pole-zero spacing.

3.2. Sensor and actuator selection

Two compact and practical sensor-actuator configurations are considered for active control law design and implementation.

Firstly, a piezoelectric patch is selected as actuator, because it can be easily integrated with the structure without any reacting base. With respect to the sensor, a piezoelectric patch for strain sensing and an

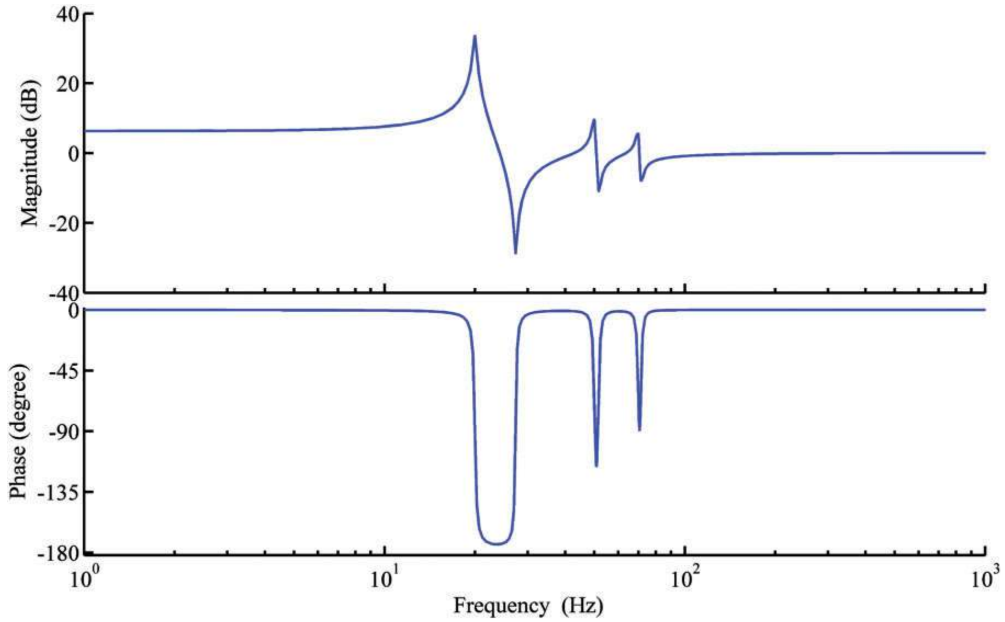

Figure 6. Bode plot of the simulated collocated transfer function.

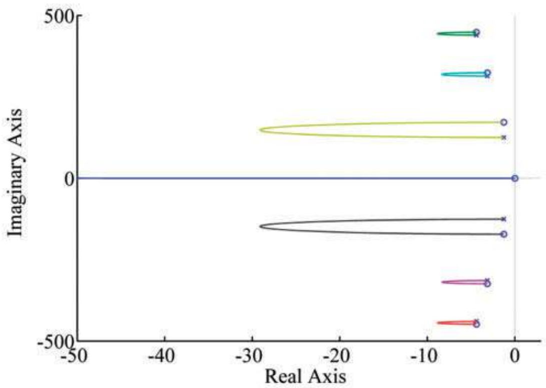

Figure 7. The relationship between zero-pole spacing and achievable maximum damping.

accelerometer for acceleration sensing should be considered.

The measured frequency response functions (FRFs) of the piezoelectric sensor-piezoelectric actuator and the accelerometer-piezoelectric actuator on the testing structure are presented in Figure 8 (the test structure is described specifically in Section 6). The measured anti-resonance points indicate zeros, and the resonance points indicate the poles of the dynamic system.

Comparing the curves shown in Figure 8, it can be easily observed that the piezoelectric sensing–piezoelectric actuating configuration has smaller zero-pole spacing than the accelerometer sensing-piezoelectric actuating configuration.

The small aperture of the collocated piezoelectric sensor can cause static response to the sensor-actuator transfer function which can then give rise to the non-uniform compliance phenomenon of the piezoelectric patch. If the panel's boundary condition is simply supported, an analytical solution of the static contribution is given in equation (10) (Vipperman and Clark, 1999). For other boundary conditions, although an analytical solution is hard to obtain, such an effect still exists, due to the fact that this phenomenon is caused by sensor and actuator.

$$\begin{aligned} G(0) = {} & \frac{16\rho_p\Theta_0^2}{k_p} \\ & \times \sum_{r=1}^{\infty}\sum_{s=1}^{\infty}\left(\frac{1}{k_r^2k_s^2}\right)\sin(k_rX_c)^2\sin(k_sY_c)^2 \\ & \times \sin\left(k_r\frac{W_x}{2}\right)^2\sin\left(k_s\frac{W_y}{2}\right)^2 \end{aligned} \tag{10}$$

where

- Θ_0 is the piezoelectric constitutive property,
- $k_r = (r\pi/L_x), k_s = (s\pi/L_x)$, with L_x by L_y the dimension of the support panel.
- W_x and W_y are the width and the length of the piezoelectric patch,
- X_c and Y_c are the piezoelectric patch's center along x- and y-coordinates,
- k_p is the piezoelectric patch's stiffness, and
- ρ_p is the piezoelectric patch's density.

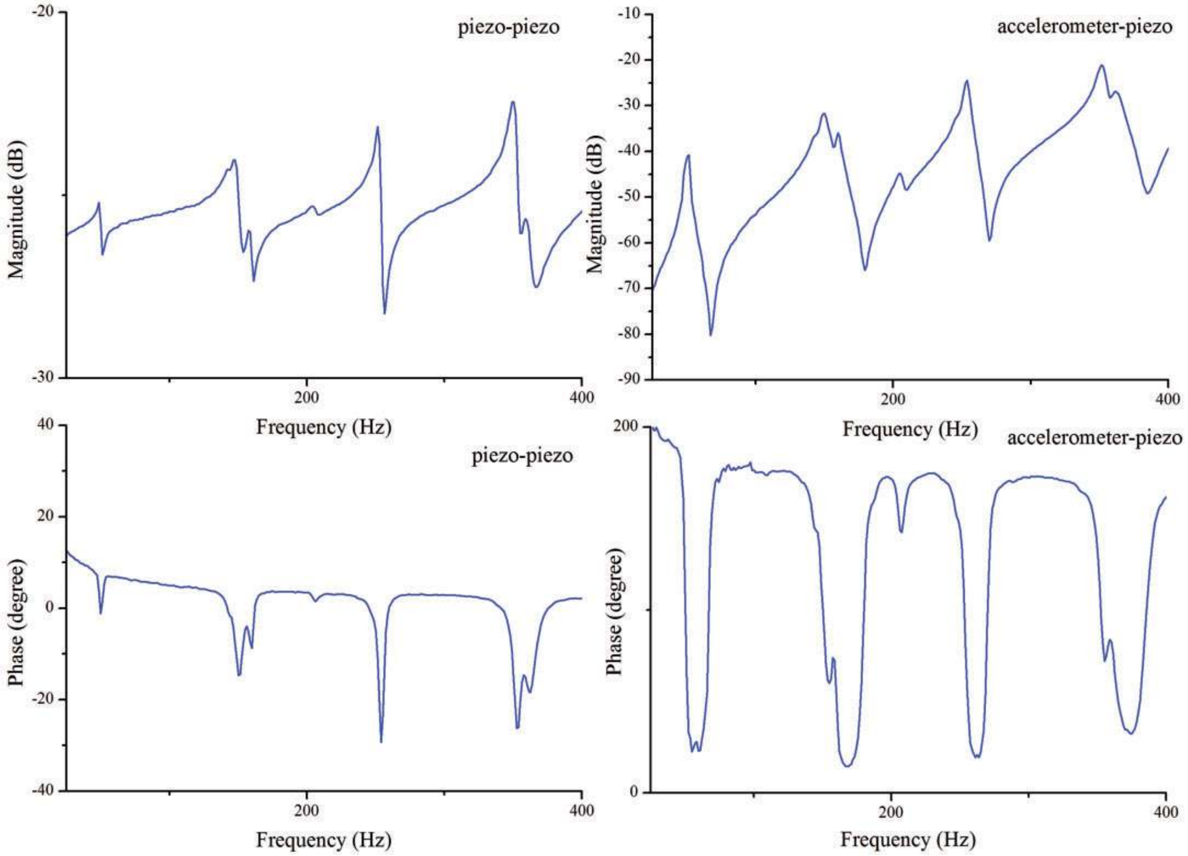

Figure 8. Measured frequency response function (FRF) curves of the piezoelectric sensor-piezoelectric actuator and accelerometer-piezoelectric actuator.

According to equation (10), this static contribution of the collocated piezoelectric patch can be taken as a feed-through item added to an ordinary transfer function, which can influence the measured FRF response, and is illustrated more intuitively by an example.

If a feed-through item is added to the transfer function of quation (9), such as:

$$\begin{aligned} G(s) = & \frac{s^2 + 2 * 0.01 * 125.6s + 29500}{s^2 + 2 * 0.01 * 125.6s + 15775} \\ & \times \frac{s^2 + 2 * 0.01 * 314s + 105000}{s^2 + 2 * 0.01 * 314s + 98596} \\ & \times \frac{s^2 + 2 * 0.01 * 439.6s + 201000}{s^2 + 2 * 0.01 * 439.6s + 193248} + 1 \end{aligned} \tag{11}$$

The Bode plots of the original system and the original system with feed-through item added are shown in Figure 9.

Comparing Figure 9 with Figure 6, the new transfer function suffers more severe pole-zero cancellation after the feed-through item is added. This indicates that the feed-through item has a great influence on the zero's locations and the close loop active damping performance.

Summarizing the above analysis, active damping performance is largely determined by the sensor-actuator's pole-zero spacing. For the piezoelectric sensor–piezoelectric actuator, due to small zero-pole spacing, this configuration will not be appropriate for low frequency active control. Conversely, with the configuration of the accelerometer sensor–piezoelectric patch actuator, as the accelerometer sensor can be deemed as an ideal sensor, a more uniform compliance can be obtained, thus much better active damping performance is anticipated. As a result, the accelerometer sensing–piezoelectric actuating configuration is selected for the following control law design and experiments.

4. Decentralized collocated feedback controller design

The decentralized control architecture with an equal number of sensors and actuators is shown in Figure 10.

For the collocated configuration, since the sensor and its corresponding actuator can use only a localized signal, the control matrix $\mathbf{H}(s)$ has a diagonal form.

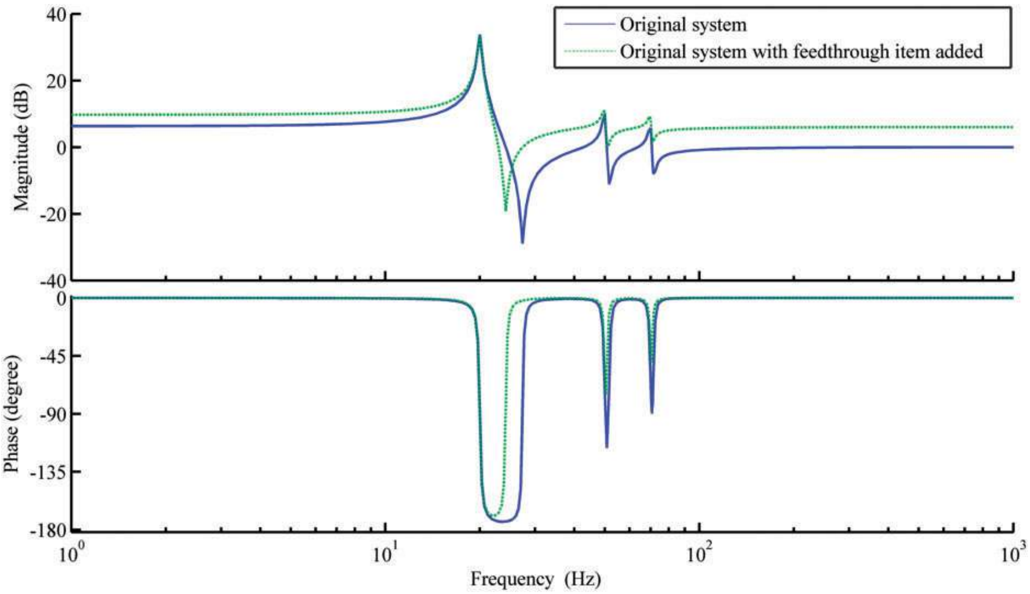

Figure 9. Bode plot of collocated transfer function with and without a feed-through item.

Thus, such a MIMO system can be decoupled into multiple SISO control loops.

Two squared matrix

$$\mathbf{G}(s) = \begin{pmatrix} g_{11} & \cdots & g_{1n} \\ \vdots & \ddots & \vdots \\ g_{n1} & \cdots & g_{nn} \end{pmatrix} \quad \text{and} \quad \mathbf{H}(s) = \begin{pmatrix} h_{11} & \cdots & 0 \\ \vdots & \ddots & \vdots \\ 0 & \cdots & h_{nn} \end{pmatrix}$$

represent the plant to be controlled and the active controller respectively. Here, the vector **y** indicates the sensors' output, and **d** is the disturbance vector. The transfer function between the disturbance and the sensor is

$$\mathbf{y}(s) = [\mathbf{I} + \mathbf{G}(s)\mathbf{H}(s)]^{-1}\mathbf{d}(s) \tag{12}$$

In equation (12), **I** is an identity matrix. Due to the diagonal property of the matrix **H**(s), the MIMO complex system has been decoupled into independent SISO loops.

Considering one of the SISO control loops, if it satisfies the condition of $|1 + G(s)H(s)| > 1$, the ratio of error signal to the disturbance signal becomes $y(s)/d(s) < 1$. Therefore, the disturbance rejection purpose is achieved. When $|1 + G(s)H(s)| < 1$, the disturbance is amplified, which means spillover occurs.

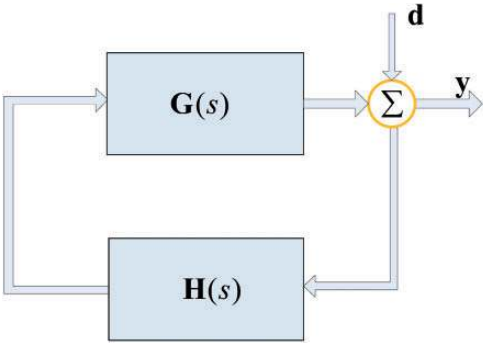

Figure 10. Decentralized feedback control architecture.

4.1. Negative acceleration feedback

For harmonic vibration control, the most notable collocated control law is PPF, in which the modal displacement signal is passed into a secondary order system to exert active damping at one specific natural frequency. Although multi-mode PPF control has been reported, the appropriate gain adjustment is rather complicated (Rew et al., 2002; den Hamer et al., 2005). As demonstrated in Section 2, more control authority should be put on the first vibration mode, which radiates the most. Therefore, we only discuss the problem of single mode PPF and its extension of NAF, which greatly simplifies the gain tuning process.

When only the first vibration mode is to be controlled, the differential equation describing the s-d.f. structure in the modal coordinate can be represented as

$$\ddot{x} + 2\xi\omega\dot{x} + \omega^2 x = f \tag{13}$$

where ω represents the structure's circular natural frequency, x is the modal displacement, ξ is the modal

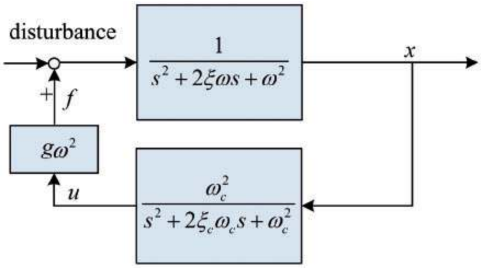

Figure 11. Block diagram of positive position feedback (PPF) controller.

damping ratio. $f = g\omega^2 u$ is the modal control force generated by the secondary actuator, with u the control signal and g the positive feedback control gain.

The PPF controller is a second-order system and its equation is shown as follows:

$$\ddot{u} + 2\xi_c\omega_c\dot{u} + \omega_c^2 u = \omega_c^2 x \tag{14}$$

Here, u is the control signal ξ_c is the damping ratio of the controller, ω_{c} is the natural frequency of the controller. In order to achieve a decent control result, ω_{c} should be the same as ω. The block diagram of PPF controller is shown in Figure 11.

According to the transformation illustrated in Section 2, the modal displacement has a proportional relationship to the physical displacement due to the equation of $\mathbf{w} = \mathbf{\Phi x}$. Therefore, the measured displacement signal can be directly used in the controller implementation.

Due to the fact that the acceleration signal is out of phase with the displacement signal, and its amplitude is ω^2 times the displacement, the modified PPF control using acceleration feedback signal can be represented as in Figure 12. Under this circumstance, the positive feedback control law changes into the NAF control law.

For example, when $\omega_c = 50$ Hz, the corresponding NAF frequency responses with different damping ratios are plotted in Figure 13. The NAF's bode plot shows clearly its dynamic properties as a typical second-order system, and helps us to discuss its control mechanism as follows.

Suppose $\ddot{x} = \alpha e^{i\omega t}, u = \beta\alpha e^{i(\omega t-\phi)}$. It can be found that β is the NAF controller frequency amplitude response, and ϕ is the phase delay introduced by the NAF controller. When $\omega \ll \omega_c$, according to the FRF property of the NAF system shown in Figure 13, $\phi \approx 0°$. Thus the compensated structure can be represented as

$$(1 + g\beta)\ddot{x} + 2\xi\omega\dot{x} + \omega^2 x = 0 \tag{15}$$

therefore the modal mass is increased.

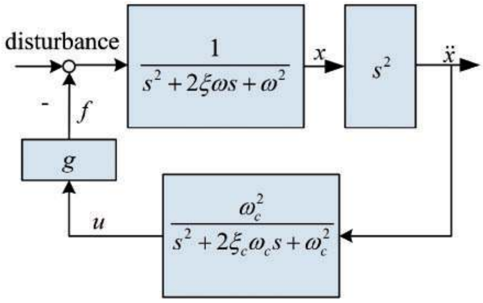

Figure 12. Block diagram of negative acceleration feedback (NAF) controller.

When $\omega = \omega_c$, $\phi = 90°$, the compensated structure can be represented as:

$$\ddot{x} + (2\xi\omega + g\omega\beta)\dot{x} + \omega^2 x = 0 \tag{16}$$

therefore the active damping is increased. Besides, as shown in Figure 13, compared with a smaller damping ratio, a larger damping ratio of the NAF controller can make smoother the phase transition at the natural frequency, which indicates that a larger damping control band can be attained.

When $\omega \gg \omega_c$, $\phi \approx 180°$, the compensated structure can then be depicted as:

$$(1 - g\beta)\ddot{x} + 2\xi\omega\dot{x} + \omega^2 x = 0 \tag{17}$$

therefore the modal mass is decreased.

Merits of NAF control law include: its control authority is focused on a specific mode, and its frequency response rolls off as high as 40 dB/dec in the high-frequencies. This can avoid high-frequency noise amplification, which is usually undesirable in the control loop. However, one major drawback is that it is not appropriate for wideband control since the controller is only targeted for one mode.

4.2. *Direct velocity feedback*

The direct velocity controller has the simplest form where the velocity signal with proper gain is feedback directly to the actuator.

$$\ddot{x} + 2\xi\omega\dot{x} + \omega^2 x = -g\dot{x} \tag{18}$$

The control item on the right side of equation (18) can be moved into the left side:

$$\ddot{x} + (2\xi\omega + g)\dot{x} + \omega^2 x = 0 \tag{19}$$

Therefore, active damping is achieved.

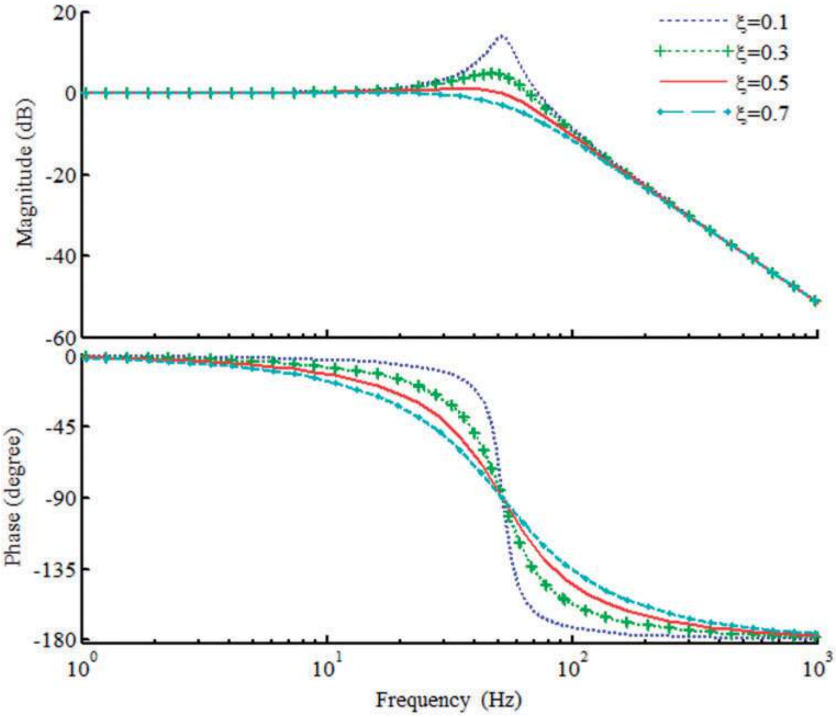

Figure 13. Bode plot of negative acceleration feedback (NAF) control with different damping ratios.

In order to obtain the velocity signal, an integral element is needed to transform the acceleration signal into the velocity signal. However, pure integration does not exist, since it has a pole at the origin. Thus, a first-order low pass filter is selected to form the electric integrator, which can generate 90 degrees phase lag above 10 Hz. The transfer function is represented as

$$H_{integrator} = \frac{1}{0.1s + 1} \tag{20}$$

The DVF controller has proven to be unconditionally stable for an idealized collocated sensor and actuator in theory (Balas, 1979; Meyer et al., 2007). With DVF control, broadband active damping can be exerted on the structure. However, for practical applications, this law has limited stability margins, which is further explained in Section 6.

4.3. Hybrid decentralized feedback

Given the considerations above, a new decentralized hybrid controller is formalized. This new hybrid controller is composed of NAF and DVF controllers. The NAF controller is used to damp the specific vibration mode which radiates the most, and the DVF controller is used to achieve broadband damping. The sensing signal is the acceleration signal, which is easy to obtain. The velocity signal can be obtained through the integrator inside the digital controller. The final control signal is the sum of NAF control law and DVF control law before the signal is sent out for D/A conversion. The proposed hybrid controller is robust and simple, and its control authority is quite reasonable. Therefore, it should be quite effective in practical circumstances.

5. Blind first natural frequency identification

From the previous analysis, the NAF controller's natural frequency should be tuned the same as the targeted structure's natural frequencies. However, the natural frequencies of physical structures may shift due to ambient environment (temperature, pressure, etc.) changes, which lead to severe degradation of the NAF control performance. Therefore it is highly recommended that before it starts to work the parameters of the controller are updated each time.

To identify the exact natural frequency, although it is feasible with the fast Fourier transform (FFT) technique, some shortcomings still exist. For instance, in order to extract accurate natural frequencies under stochastic broad spectrum excitation, a large amount of data is needed to get high-frequency resolution. Besides, windowing is needed to reduce leakage and requires repeated averaging to eliminate noise. In summary, this method is time-consuming and cannot cope well with the non-stationary signal.

To overcome those drawbacks, the Hilbert-Huang method (Huang et al., 1998) is introduced. This method is based on empirical mode decomposition (EMD) and only needs a short structural response signal for blind identification. Based on this spectral analysis, the first-order natural frequency can be extracted easily and accurately for the NAF control law implementation. Although the Hilbert-Huang analysis has been successfully used in many areas, it has rarely been used for active control application.

The basic principle of Hilbert-Huang natural frequency identification is that using the EMD the vibration signal can be decomposed into intrinsic mode functions (IMFs), which correspond to the structural vibration modes. Then the time-frequency information can be obtained through Hilbert transformation of IMF, where each IMF admits well-behaved Hilbert transformation, and the natural frequency can be extracted from the measured vibration response signal (Yang et al., 2003a,b).

The general process to extract the first natural frequency can be summarized as follows:

1. The rough band where the first natural frequency locates is determined. Then a bandpass filter is used to preprocess the response data detected by the sensor. This can greatly enhance the signal-noise ratio (SNR) and simplify the computation efforts. As the natural frequency may shift, the bandpass filter should have a proper band. For our experiment, the filter's bandwidth is set to be 20 Hz.
2. The vibration signal is decomposed into IMFs. After the decomposition, the original signal can be reconstructed by the IMFs and the residues.
3. The instantaneous frequency can be obtained after the Hilbert transformation of IMFs. Assuming the structure is linear, the natural frequency should be constant. However, the instantaneous frequency usually has some fluctuations due to the non-stationary excitation. Therefore, a median filter is used to filter the instantaneous frequency sequence, and the median frequency is selected as the identified natural frequency. The averaged instantaneous frequency sequence is not adopted due to the endpoint effect (Huang et al., 1998), which may generate a big instantaneous frequency fluctuation and add a bias to the true frequency value in real circumstances.
4. When the first natural frequency is identified, this frequency is sent to the real-time (RT) controller, and active control starts to work.

6. Experimental system setup and open-loop analysis

6.1. Test structure arrangement

To investigate the proposed hybrid control law, an experiment is carried out in the following sections.

Firstly, a test structure is needed to justify the effectiveness of the proposed control law for sound transmission control. Such a structure is designed and built up by the following three components:

1. An aluminum plate with a thickness of 1 mm, which is used for sound transmission control;
2. An aluminum frame formulated near clamped boundary conditions, which restricts the plate's movement;
3. A polymethyl methacrylate (PMMA) cavity inside of which a loudspeaker is placed for noise transmission problem study. The PMMA panel, whose thickness is 50 mm, could provide more than 30 dB sound isolation in the low frequency band, and thus is correct to evaluate the final active control performances.

The physical parameters of the test structure are shown in Table 1.

Referring to the conclusions in Section 2, the sensor-actuators should have the maximum coupling at the most sound radiation efficiency modes, which are odd-odd modes. Therefore, three pairs of patches are boned on the middle part of the panel. This location is determined by experimental modal analysis results, which ensures the system's controllability and observability at the interested modes. Each pair is boned symmetrically so that it can generate a pure moment to the plate. That is, when one patch stretches the other will compress under the control voltage of the power amplifier. The patch's physical parameters are shown in Table 2. The miniature accelerometers (type PCB 352A56) are adhered to each of the piezoelectric patch's upper side. Such a configuration makes the piezoelectric pair and the accelerometer a collocated sensor-actuator form, as shown in Figure 14.

To evaluate sound radiation reduction performance, the active control experiment is carried out in an anechoic chamber. A photograph of the experimental setup is shown in Figure 15. Three 1/4 inch microphone sensors (GRAS 40 ph, 50 mv/Pa), placed 0.5 m away from the plate, are used for sound pressure monitoring. The NI Sound and Vibration toolkit is used to analyze the sound data.

6.2. Fluid-structure analysis of the test structure

The influence of acoustic source location to the plate's response should be investigated. Because such analysis has rarely been carried out in active control research, it is very helpful to reveal the relationship of the structure response and the acoustic excitation inside the cavity.

Finite element analysis is the correct way to solve such a problem, which involves the 2-D plate elements and the 3-D acoustic elements. The finite element sizes are selected to be small, which can be accurate enough up to 1 kHz. The cavity's dimension is 420 mm × 420 mm × 365 mm and the plate dimension is 420 mm × 420 mm × 1 mm. These dimensions are set to be the same as shown in Section 6.1. MSC ACTRAN software is used to generate the computation results which are needed for the following analysis.

Table 1. Parameters of the test structure.

Components	Parameters
Actual volume of the cavity	420 mm × 420 mm × 365 mm
Thickness of the aluminum	1 mm
Dimensions of the outer frame	480 mm × 480 mm
Dimensions of the inner frame	420 mm × 420 mm
Thickness of the PMMA	50 mm
Poisson ratio of the aluminum	0.33
Young's module of the aluminum	70 GPa
Density of the aluminum	2700 kg/m^3

PMMA: polymethyl methacrylate.

Table 2. Physical properties and geometric data of the PZT patch.

Components	Parameters
Length	40 mm
Width	40 mm
Poisson ratio	0.39
Density	7600 kg/m^3
Thickness	1 mm
Piezoelectric constant d_{31}	-270×10^{-12} C/N

Firstly, the acoustic modes' natural frequencies of the cavity can be extracted under the modal acoustic solution. In this case, each side of the cavity is supposed to be infinitely rigid and the fluid in the cavity is supposed to be perfect gas. The finite element mesh size is selected as 50 mm, and the total number is 1966, which can guarantee that the acoustic wavelength comprises at least six elements till 1 kHz.

The acoustic modes' natural frequencies (between 1–1 kHz) and the corresponding sound pressure distributions inside the cavity are shown in Figure 16:

Secondly, the influence of acoustic distribution needs to be investigated. According to the acoustic modes information, below 400 Hz, there is no acoustic resonance in the cavity. In the low frequencies, because the acoustic wavelength is much bigger than the dimension of the plate, the disturbance phase distribution is relatively constant over the plate surface. For instance, at 100 Hz, the acoustic wavelength can be as long as 3.4 m.

Thus, in the low frequencies, it can be anticipated that there should not be a significant difference in the response of the plate when the location of loudspeaker is changed. Besides, the volumetric modes tend to couple more efficiently than other modes.

To prove the above analysis, the plate's 2-D mesh is now added to the cavity's top surface, which mimics the real circumstance shown in Figure 15. The plate is aluminum, and the structural damping is assumed to be 2%. The element's edge length is 1 cm and the element number is 1764. In addition, another 3-D acoustic volume mesh with a dimension of 1.4 m × 1.4 m × 0.55 m is put on the top surface of the plate, and the element number is 25829. Infinite acoustic

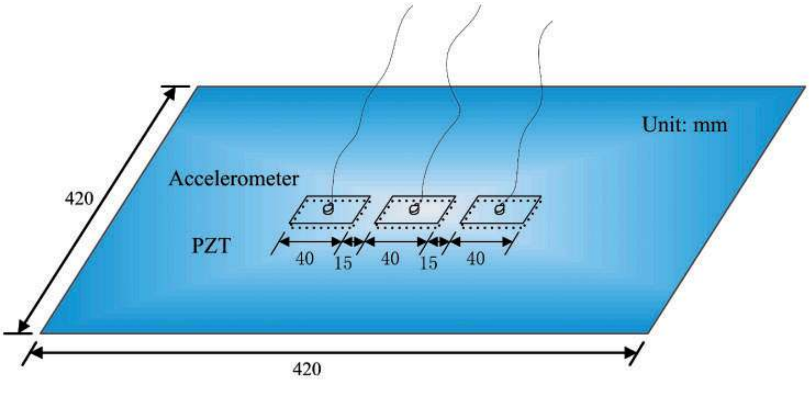

Figure 14. Schematic diagram of the sensors and actuators arrangement for active control experiments.

elements are generated on the surface of the acoustic volume mesh.

The acoustic finite elements are used to capture the near field sound information and the acoustic infinite elements are used to mimic non-reflecting boundary conditions and capture the far field sound information. Virtual microphones are added to the acoustic domain and the panel's sound radiation power can be calculated according to the standard ISO 3744 method. Coupling manipulation is carried out to link the different property element sets. The direct frequency response solution is adopted to analyze the plate response in the frequency 1–500 Hz. The computation step is 0.2 Hz. The acoustic excitation is represented by a spherical point source, which has amplitude of 1 Pa. The final computation model is shown in Figure 17.

Four load cases are carried out. In each case, the acoustic source is located at different places inside the cavity illustrated in Figure 18: Case 1: center point of the cavity (0.21,0.21,0.15); Case 2: one corner point of the cavity (0.42,0.42,0.05); Case 3: along one side of the cavity (0.21,0,0.05); Case 4: arbitrary point inside the cavity (0.30,0.17,0.15).

Finally, the mean square velocity of the entire panel and the panel's sound radiation power according to ISO 3744 standard are shown in Figures 19 and 20. According to these computation results, the plate responses' trends under different locations of acoustic excitation are almost the same in the low frequency. The odd-odd modes play a major contribution in the sound power spectral. Although other resonances can be observed in the vibration domain, for instance, at 100 Hz (1,2 mode), such a mode has little contribution to the sound power radiation. One reason is this mode couples weakly with the acoustic excitation. As shown in Case 1, this mode cannot even be excited when the acoustic source is located in the center of the cavity. Another reason is its radiation efficiency is low, which has little influence on the global sound radiation power, as shown in Figure 20. Therefore, the simulation results justified the acoustic source's location has little influence to the structure's response. It also indicates using limited sensor and actuator could reduce the interesting mode's vibration and sound radiation. At higher frequencies, due to the existence of acoustic resonance and mode shapes becoming more complex, it is anticipated that active damping performances will be limited.

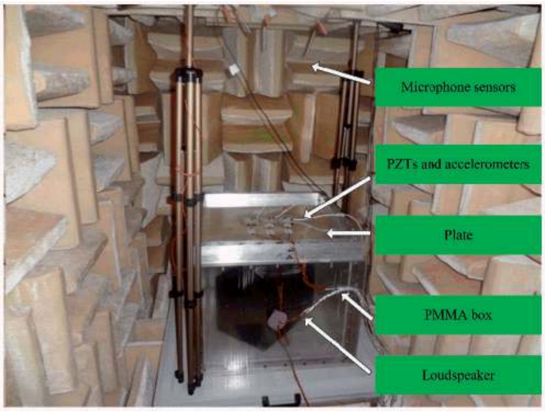

Figure 15. Photograph of the test structure and the anechoic chamber.

Remark: It is known from some of the literature that when the loudspeaker is very close to the plate, at a location 1/4 edge length away from the plate, the (1,2) mode or the (2,1) mode can be well excited. Besides, because the (2,2) modes radiate the least, it can be omitted. Therefore, the three sensor/actuator pairs can be used to control the (1,1) mode, (1,2) mode and (2,1) mode independently. In this paper, because we did not take this special case in our following experiments, the (1,2) mode and the (2,1) mode are not well excited.

6.3. Open-loop analysis

First of all, the selection of the sampling rate for broadband feedback control is considered. There is a data sampling and conversion process (A/D and D/A) in the digital control loop. The total delay caused by the A/D and D/A conversion can be approximated as e^{-2sT}, where T is the sampling interval. Apparently, a large value of T results in a substantial phase lag at high frequencies, and may lead to spillover or instability in the feedback loop.

Therefore, the measurement of the A/D to D/A's magnitude and phase responses with different sampling rates are given in Figure 21. This figure shows clearly that the sampling rate can significantly influence the audio-frequency feedback control. For instance, at the frequency of 1 kHz, the phase lag with the sampling rate of 2 kHz can be as large as 100 degrees, which is obviously unacceptable in the feedback loop. However, when the sampling rate is increased up to 20 kHz, the phase lag is no more than 16 degrees. Such a small delay is acceptable if the control bandwidth is within 1 kHz. Therefore, a 20 kHz sampling rate is selected for the following active control experiments.

With such a high sampling rate, however, another problem arises. High loop rates of such RT tasks usually demand expensive and intensive power consumption processors. This will increase the system's cost and make it bulky. Fortunately, Field Programmable Gate Array (FGPA) technology (Antila, 2004) is becoming a

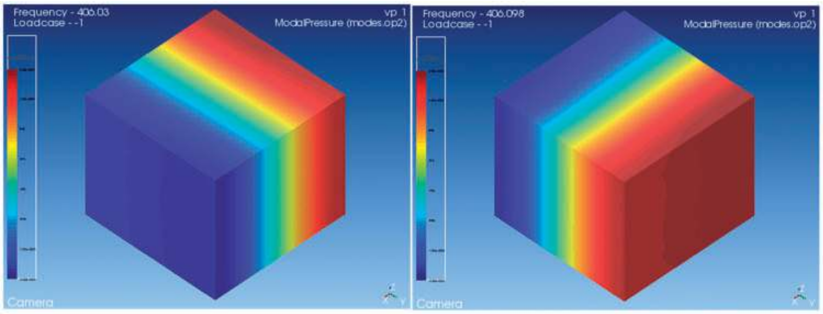

Mode 1 406.030 Hz

Mode 2 406.098 Hz

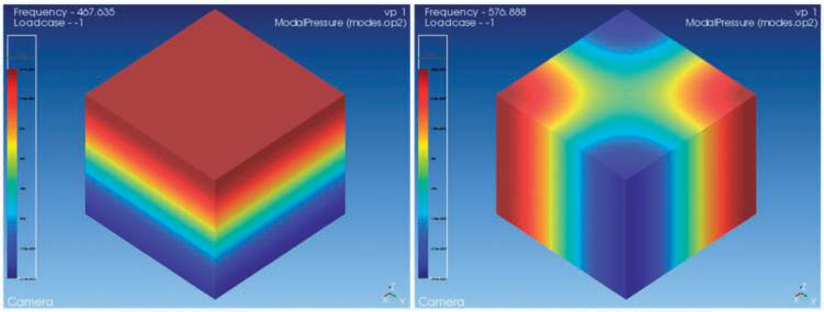

Mode 3 467.635 Hz

Mode 4 576.888 Hz

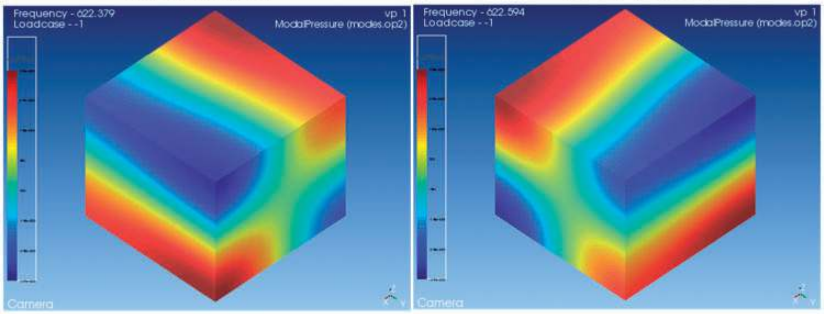

Mode 5 622.379 Hz

Mode 6 622.594 Hz

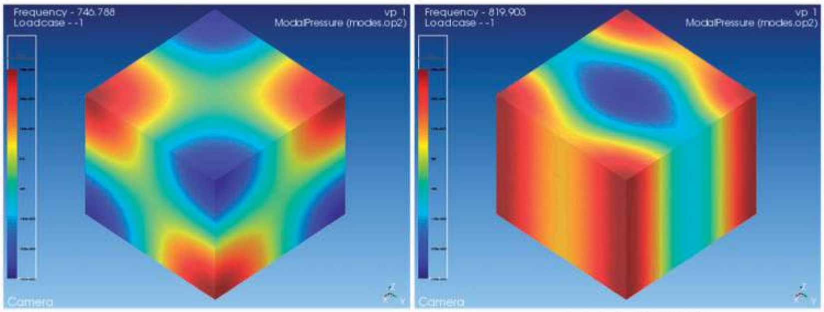

Mode 7 746.788 Hz

Mode 8 819.903 Hz

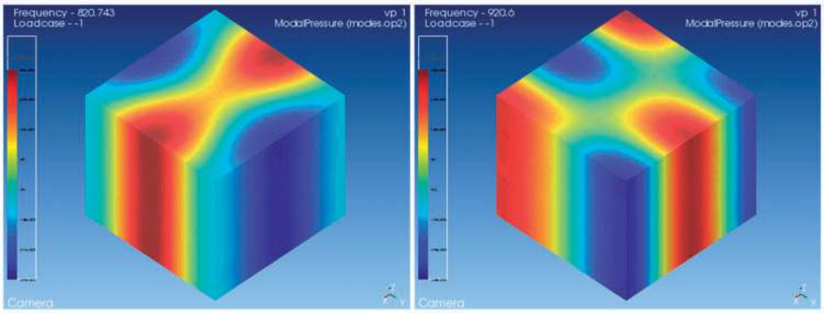

Mode 9 820.743 Hz

Mode 10 920.600 Hz

Figure 16. Acoustic mode shapes of the cavity.

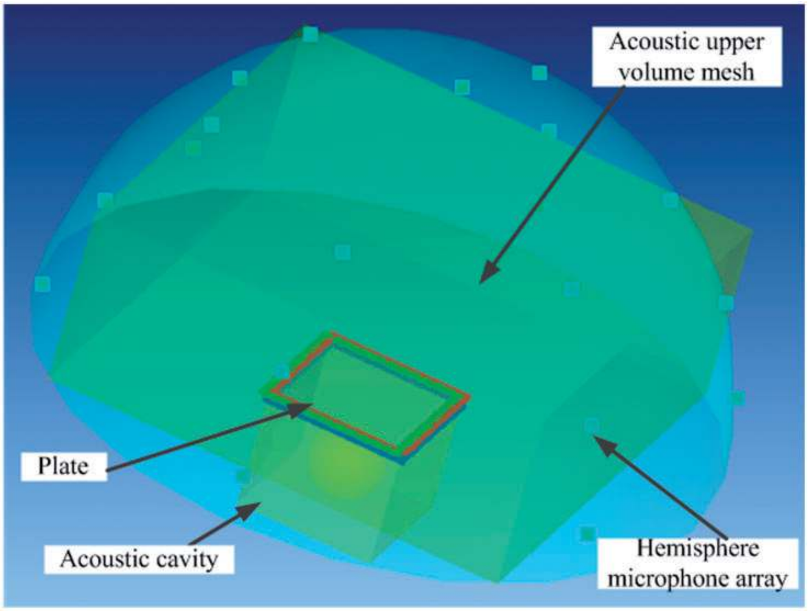

Figure 17. Computation model.

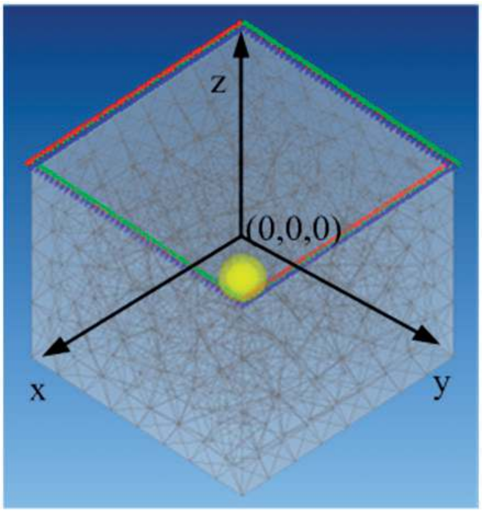

Figure 18. Coordinates definition used to define the acoustic source location.

powerful approach to solve the above dilemma. Control algorithms can be compiled and implemented in programmed digital electric circuits, which enable the control algorithms to run in parallel, and which ensure a deterministic control with high loop rates but low power consumption.

For this reason, a Xilinx Virtex-5 LX110 FPGA chip, which is embedded on an NI CRIO 9118 target, is selected for our control algorithms' implementation. The CRIO system also comprises an embedded 800 MHz PowerPC RT controller for data monitoring and control results evaluation. The Hilbert-Huang algorithm is implemented on the RT controller by direct memory access (DMA) data communication, and the identified natural frequency of the first mode is sent to the FPGA target.

Finally, there are also some delays in the feedback loop which are not easy to eliminate. These delays are mainly caused by dynamic responses of the analog filters and other electronic components and distance from the piezoelectric actuator to the accelerometer. Therefore, an open-loop system frequency response measurement is taken for stability analysis and the schematic diagram of the open-loop frequency response measurement is shown in Figure 22.

Under DVF control, the measured Nyquist plots with the excitation bandwidth of 0–1 kHz and 0–2 kHz are shown in Figure 23.

The corresponding Bode plots are shown in Figure 24.

Theoretically, the DVF control law exerted on the collocated system is unconditionally stable, which means that the Nyquist plot should be located on the right half of the complex plane where the phase response in the Bode plot varies within the range of $-90^\circ \sim 90^\circ$. However, according to Figures 23 and 24, it can be seen clearly that if the excitation frequency band is higher than about 1.42 kHz, the Nyquist plot may enter the left side of

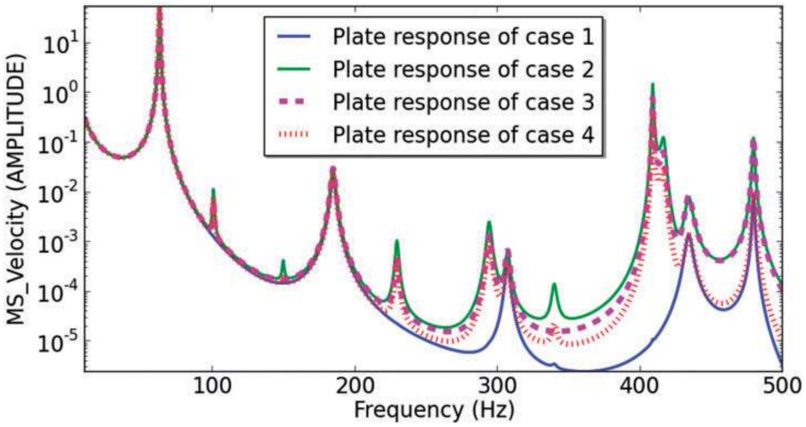

Figure 19. Mean square velocity of the plate under different case load loads.

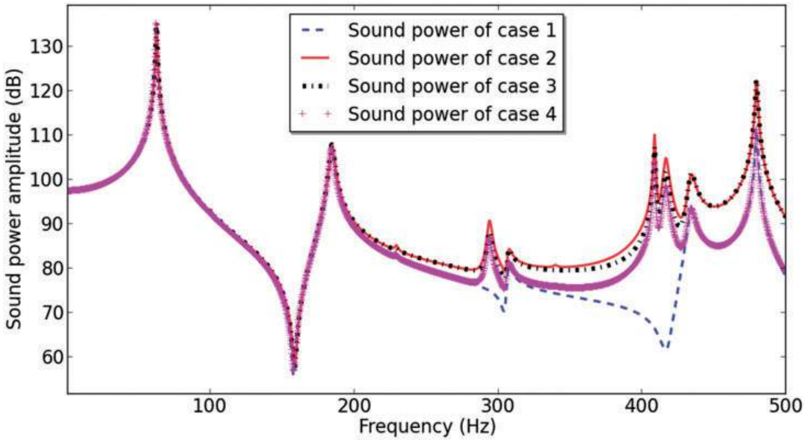

Figure 20. Sound radiation power according to ISO 3744 standard under different case loads.

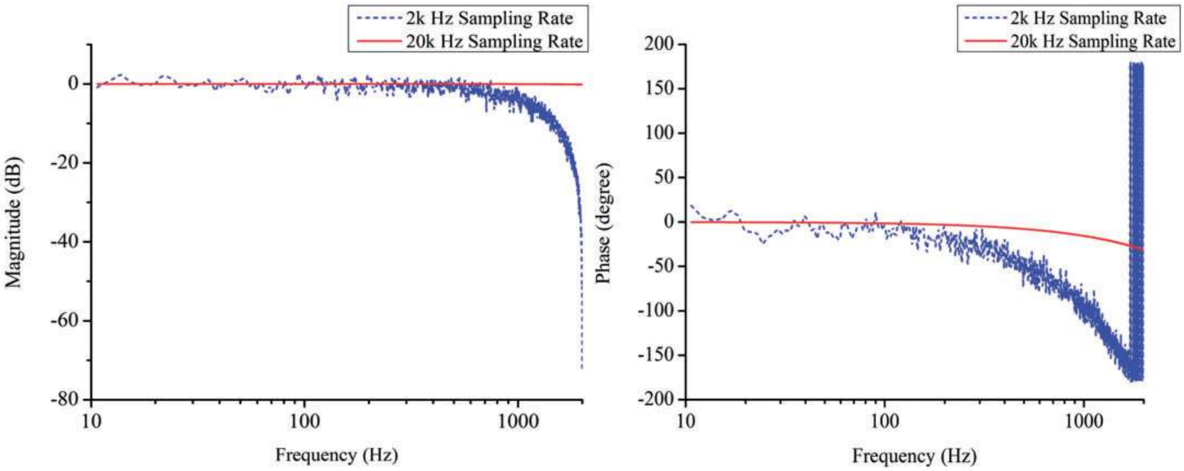

Figure 21. Measured A/D- D/A magnitude responses and phase responses with different sampling rates.

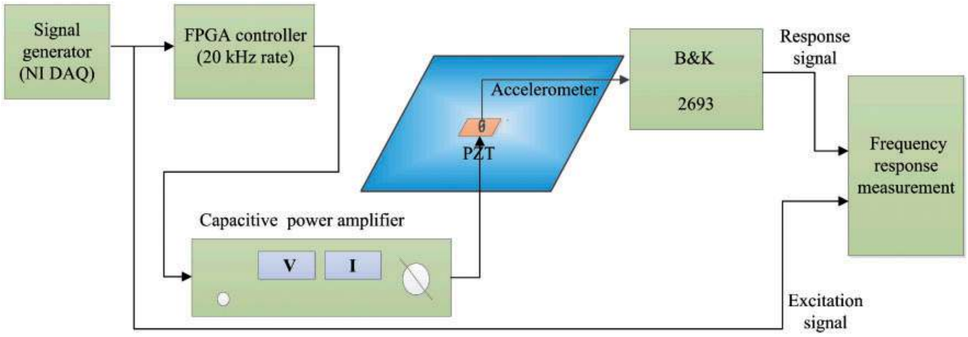

Figure 22. Schematic diagrams of the open-loop frequency response measurements.

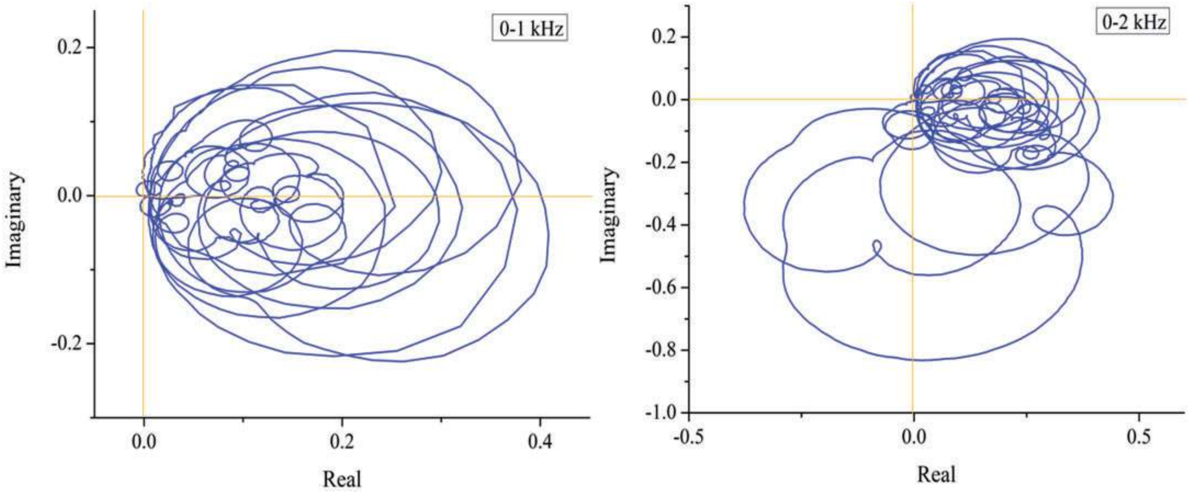

Figure 23. Measured Nyquist plots of direct velocity feedback (DVF) control with different disturbance bands.

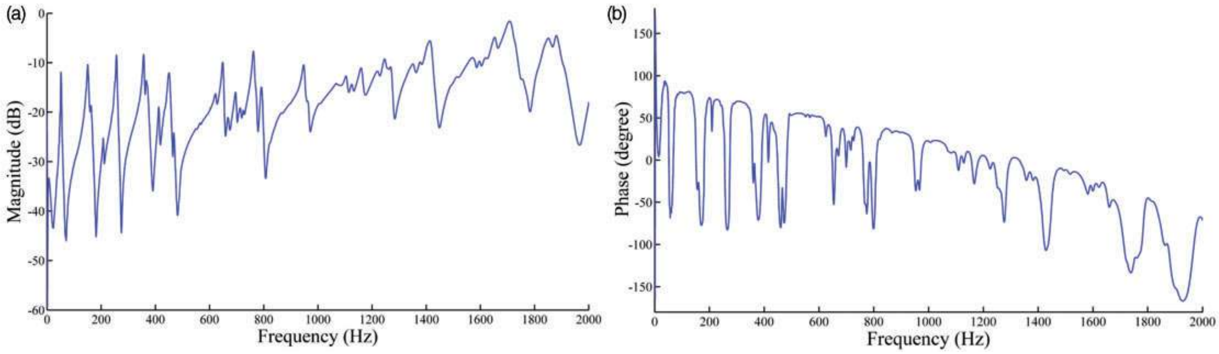

Figure 24. Measured open loop Bode plots of direct velocity feedback (DVF) control.

the Nyquist plane. Due to the time delay in the feedback loop, the whole system is only a band-limited minimum plant under real circumstances. In consequence, if the control gain is high enough, the Nyquist plot will finally encircle the point of $(-1, j0)$, which indicates instability.

The measured Nyquist plots with the excitation bandwidth of 0–1 kHz and 0–2 kHz under NAF

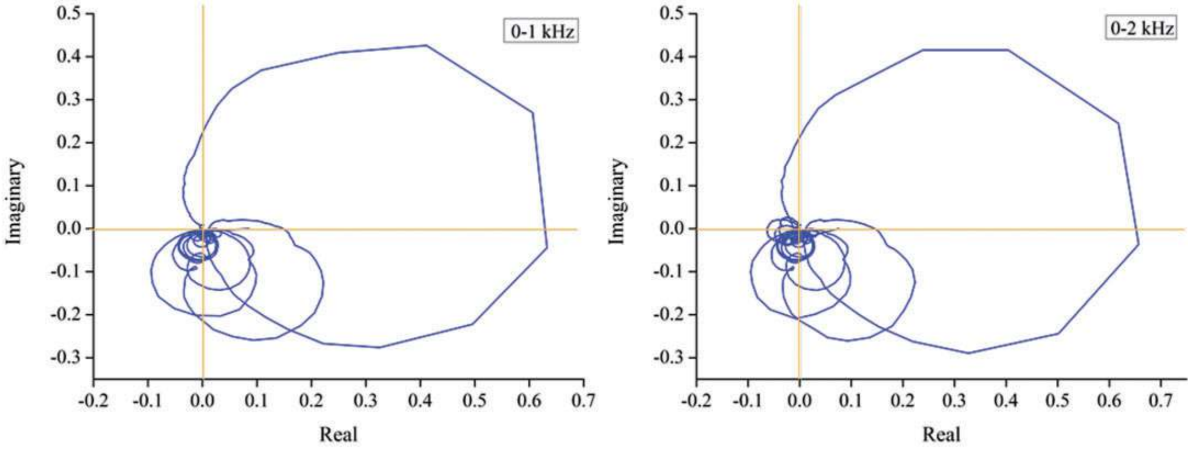

Figure 25. Nyquist plots of negative acceleration feedback (NAF) control with different control bands.

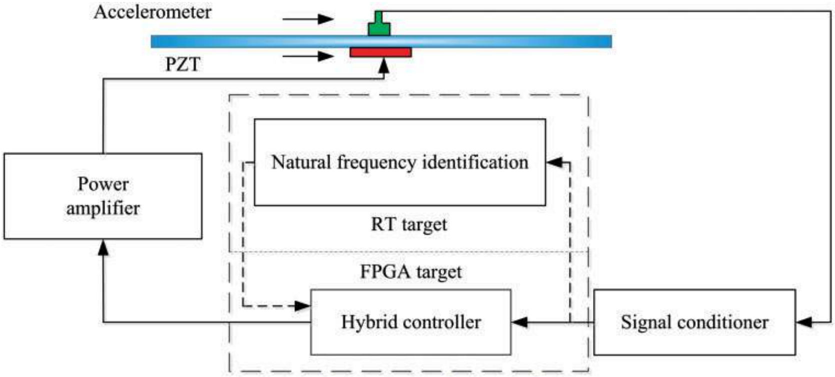

Figure 26. Schematic diagram of the decentralized control loop process.

Table 3. Identified first natural frequency results by the Hilbert-Huang method.

1	2	3	4	5	6	7	8
50.22 Hz	49.51 Hz	49.67 Hz	50.01 Hz	49.90 Hz	49.97 Hz	50.14 Hz	50.06 Hz

control are shown in Figure 25. The targeted control frequency (50 Hz) corresponds to the biggest circle in the Nyquist plot. At higher frequencies, the Nyquist plots locate mainly in the range of $-0^\circ \sim -180^\circ$ because of the phase lag caused by the NAF controller. Due to the roll-off of the NAF controller, circles' diameters in the high frequency are much smaller than those in the DVF Nyquist plot, which indicates that the NAF controller is more robust than the DVF controller. For this reason, the hybrid control law's robustness will be no worse than the DVF controller alone.

7. Closed-loop experimental results and analysis

The complete procedure for the first natural frequency identification and active control can be summarized as follows, with a schematic chart given in Figure 26.

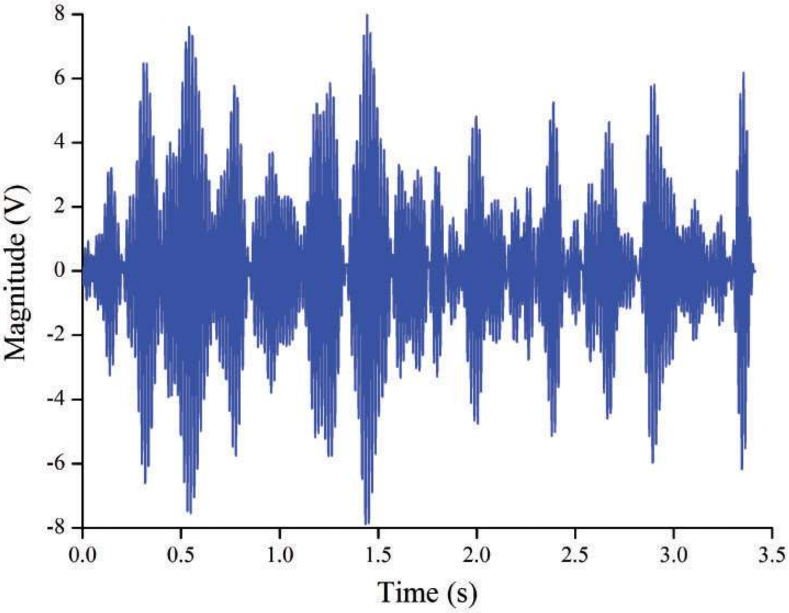

Figure 27. One group of measured data used for the first natural frequency extraction.

1. A band-limited white noise is used to excite the plate structure. This white noise ranges from 30 Hz to 1000 Hz and is generated by a loudspeaker inside the PMMA cavity.
2. The response signals sensed by the middle accelerometer sensor are sampled and transferred to the RT target.
3. The first natural frequency is extracted through the Hilbert-Huang algorithm on the RT target.
4. The identified first natural frequency is sent to modify the NAF controller's parameters on the FPGA target.
5. Active control is approved to start.

When the identification procedure starts, the sampling rate is 3 kHz and the duration of sampling is 3.4 seconds. Then the measured acceleration data are sent into a fourth-order bandpass filter ranging between 40 and 60 Hz. In order to test the Hilbert-Huang method, eight measurements are taken and the identified natural frequencies are listed in Table 3.

Figures 27 and 28 illustrate one group of measured data and their corresponding instantaneous frequencies obtained by the Hilbert-Huang analysis.

The natural frequency identified by exponential average FFT with a frequency resolution of 0.2 Hz is 50.0 Hz. Compared with the FFT method, the proposed Hilbert-Huang method is accurate enough. The computation takes about five seconds on the RT target, which is much faster than the average FFT refinement, which takes more than one minute.

The controller' gain tuning is related to the type of sensing signal. NAF control law uses the acceleration signal directly, whereas the DVF control law uses the velocity signal, which is the integral of acceleration. For this reason, the DVF's gain should be much larger than the NAF's so that control law gives sufficient control authority to the piezoelectric patch at low frequencies.

The gains of NAF and DVF may have an optimal relation. However, such a relation is difficult to find in real experiments. The main reason is that the results are largely determined by instrumentation factors, as suggested by Gatti et al. (2007). Those factors include instrument noise, A/D and D/A conversion errors, power line interferences, imperfect sensor/actuator pairs, built-in filters in the signal conditioner, etc. All of them are difficult to model and to predict.

Therefore, a more conservative solution is adopted in our experiment. Firstly, the frequency responses of the NAF and that of the integration filter are examined. Secondly, every controller's output amplitude is set to be equal at 50 Hz, a value which is around the structure's first natural frequency. To this end, the DVF's gain is set to be 30 times larger than the NAF's. Such a gain tuning method is effective for both narrowband and wideband control. The final Bode plots are shown in Figure 29.

Figure 29 shows that, at 1.42 kHz, the NAF's magnitude is almost 30 dB lower than the DVF's. As a large

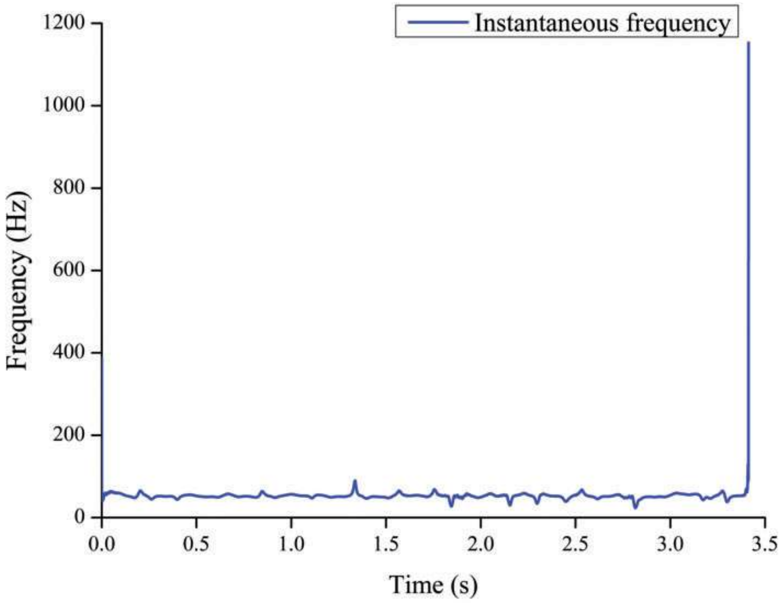

Figure 28. Corresponding calculated instantaneous frequency using the Hilbert-Huang method.

gain will give rise to spillover and instability at higher frequencies, the NAF is more robust than the DVF.

The DVF provides only a damping effect to the structure, whereas the NAF can also change the structure's modal mass. Consequently, when the gain of NAF control is too large, the target mode will shift, which will deteriorate the control result. With the hybrid control gain turning proposed above, the NAF is stable provided that the DVF is stable. Because the DVF control law exerts wideband control authority, with the proposed hybrid control, performance enhancement on the first vibration mode and the wideband control can be achieved simultaneously.

Figure 30 shows the average acceleration signal's power spectrum without any control, with NAF control, with DVF control, and with NAF + DVF control. The damping ratio of the NAF controller is set to be 0.5.

As seen in Figure 30, with the NAF active control, the reduction at the first natural frequency (1,1 mode) is 13.6 dB. The adjacent mode's natural frequency shifts a little due to the modal mass change which has been described in Section 4. At higher frequencies, owing to the roll-off property of the NAF controller, there is almost no difference compared to the original spectrum. In the case of DVF control, the magnitude of the first vibration mode is reduced by 9.98 dB. Although this reduction is smaller than using NAF control, the DVF controller has a broadband control authority. For instance, the 158 Hz vibration mode's magnitude (1,3 mode) has been reduced by 12.6 dB. At other frequencies, 10 dB reduction at 252 Hz, roughly 4–5 dB reduction at 340 Hz, 357 Hz, 652 Hz and 922 Hz are observed, etc. This suggests that the two control methods are complementary.

The hybrid control has a better control performance than the DVF control at the 1,1 mode, and a better performance than NAF control at all vibration modes. For instance, at the first vibration mode, the reduction is 16.71 dB, which is 6.73 dB higher than using DVF control and 4.11 dB higher than NAF.

In the frequency band of 400–500 Hz, as shown in Figure 30, the active control seems to have little effect. This is because under this circumstance, the cavity acoustic modes have strong coupling with the structural modes, which has been anticipated in Section 6.2. The acoustic mode at 467.635 Hz has the biggest influence on the upper aluminum panel. Its mode shape is shown in Figure 16.

Thus, the poor control performance around this frequency band could be explained by the resonance of the cavity beneath the panel. Better control results are anticipated when the strong coupling between the cavity and the plate are eliminated.

Figure 30 also shows that, the high frequency vibration effectiveness is not as good as that at low frequencies. This is because of the use of limited sensor/actuator pairs, which may locate on the nodal lines of high-order modes.

The measured time-domain acceleration signals without and with hybrid control are compared in

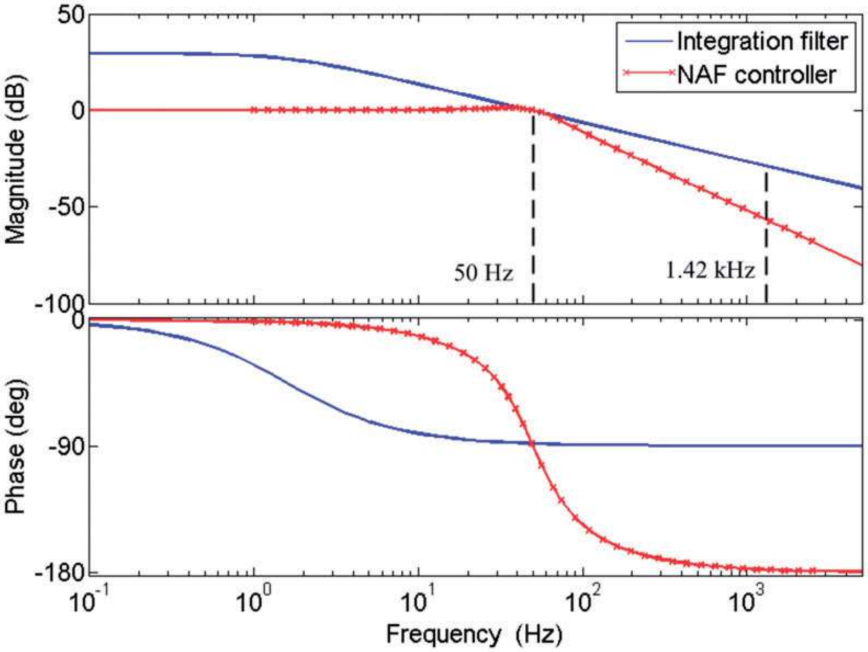

Figure 29. Bode plots of the integration filter and negative acceleration feedback (NAF) control law with a gain ratio of 30.

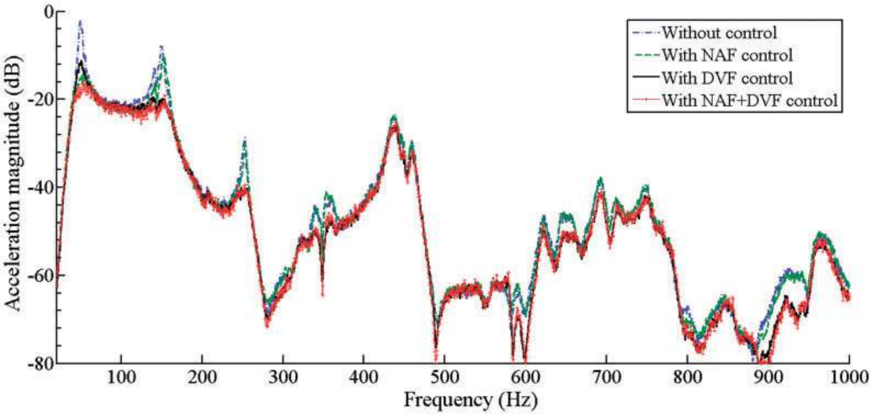

Figure 30. Measured acceleration spectrum response of the controlled and uncontrolled plant.

Figure 31. It can be seen clearly from the figure that the vibration level has been attenuated dramatically using the hybrid controller.

The average sound pressure level (SPL) spectrum before and after control is shown in Figure 32. The SPL attenuation trend in this figure is similar to the acceleration signal reduction trend in Figure 30. The 1,2 mode (85 Hz) and 2,2 mode (132 Hz) have little contribution to the global sound pressure level.The suppressions of dominant radiation modes are quite significant: more than 15 dB at the 1,1 mode and nearly 10 dB at the 1,3 mode are reduced. These control results also indicate that the proposed controller can not only suppress the kinetic energy of the vibrating structure but can also increase the sound isolation performance.

Finally, the global sound pressure level reductions in the range of 30–1000 Hz are summarized in Figure 33.

Without control, the overall SPL in the frequency band of 30–1000 Hz is 72 dB. The global magnitude reduction is 5 dB with NAF control, 5.5 dB with

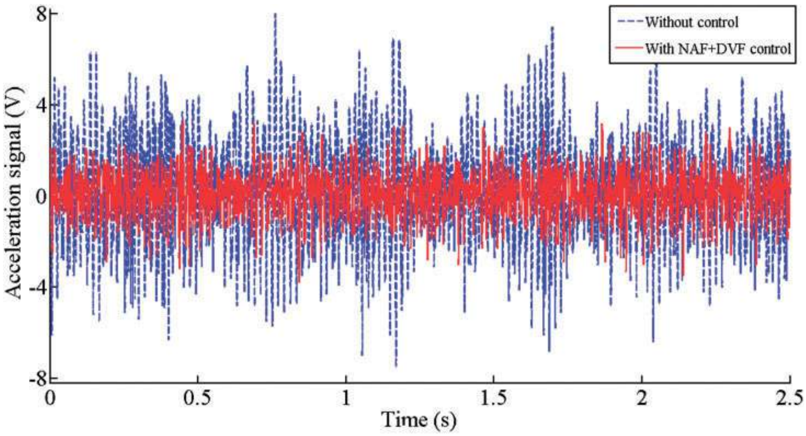

Figure 31. Measured time domain acceleration signal without control and with hybrid control.

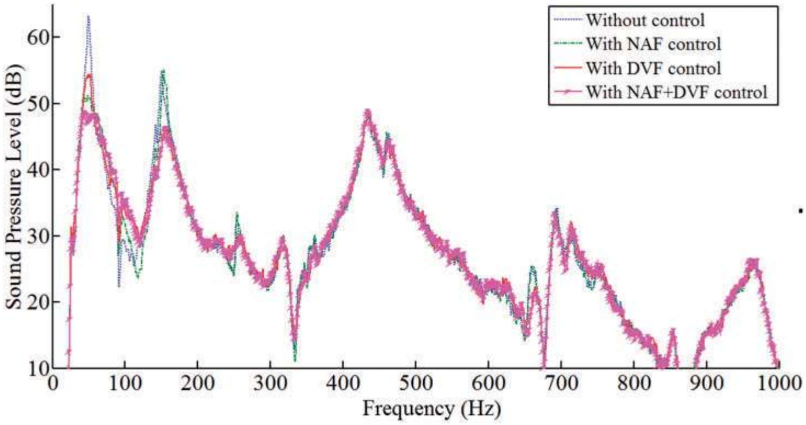

Figure 32. Measured sound pressure level spectrum response of the controlled and uncontrolled plant.

DVF control, and 7.5 dB with NAF + DVF hybrid control.

8. Conclusion

In this paper, the active control of an aluminum panel for sound transmission using a hybrid control law is investigated. The actuator type is PZT. To maximize the active damping effect, accelerometers, rather than PZT patches, are adopted as sensors. The decentralized control architecture ensures that other control loops are still able to work even if one of them fails. Then a hybrid control law which can properly exert active damping on the panel is derived. In the hybrid control method, the DVF control law is used for broadband control and the NAF control law is used for narrowband control. The NAF has the feature of rolling off quickly at high frequencies, which assures its robust performance. The mechanism and property of each control law are illustrated explicitly. As the NAF has an active damping effect only when its natural frequency is tuned the same as the structure's, the latter is the only parameter that should be known. The Hilbert-Huang method is adopted to extract the structure's first natural frequency automatically and effectively under non-stationary excitation. The identification procedure requires only a small amount of the time domain structure's response data every time the active controller starts to work. The aspects of implementation are considered in detail, and finally a parallel high-speed three-channel controller is constructed with the help of modern FPGA technology. The control results verified the effectiveness of the proposed control method. The target odd-odd modes have been significantly suppressed. However, the control performance is less effective for higher modes due to

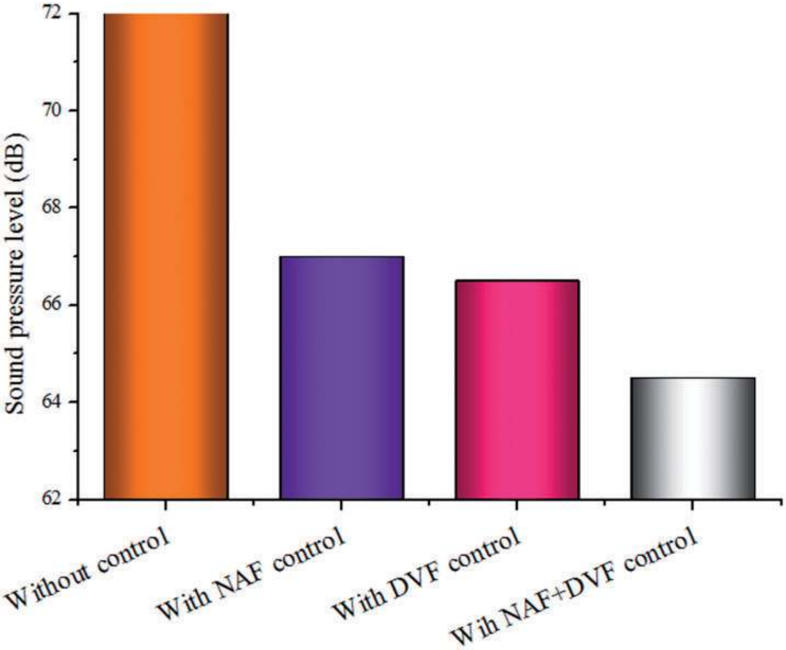

Figure 33. Average sound pressure level (SPL) global reductions.

the cavity resonance and limited sensor/actuator pairs. Therefore, for further suppression of high-order vibration modes, the use of idealized acoustic excitation, combined with porous material/viscoelastic layer are recommended. The proposed hybrid control law here also suggests that other kinds of hybrid control laws could also be promising and are thus worth further research.

Acknowledgements

The authors sincerely thank the reviewers for their valuable comments and suggestions, which have led to the present improved version.

Funding

This work was supported by the Program for Changjiang Scholars and Innovative Research Team in University (grant number IRT0968), PAPD, the China Scholarship Council, the National Natural Science Foundation of China (grant number 51375228), the Postdoctoral Science Foundation (grant number 2012M521082), the Doctoral Fund of Ministry of Education of China (grant number 20123218120035) and the Funding of Jiangsu Innovation Program for Graduate Education (number CXLX11_0186).

References

Antila M (2004) Contemporary electronics solutions for active noise control. *Proceedings of International Symposium on Active Control of Sound and Vibration*, ACTIVE 2004, Williamsburg, VA, USA, 20–22 September 2004.

Aphale SS, Fleming AJ and Moheimani SR (2007) Integral resonant control of collocated smart structures. *Smart Materials and Structures* 16: 439–446.

Balas MJ (1979) Direct velocity feedback control of large space structures. *Journal of Guidance, Control, and Dynamics* 2: 252–253.

Berry A, Guyader JL and Nicolas J (1990) A general formulation for the sound radiation from rectangular, baffled plates with arbitrary boundary conditions. *The Journal of the Acoustical Society of America* 88: 2792–3202.

Chen Y, Zimcik DG, Wickramasinghe VK, et al. (2004) Development of the smart spring for active vibration control of helicopter blades. *Journal of Intelligent Material Systems and Structures* 15(1): 37–47.

Choi S-B (2006) Active structural acoustic control of a smart plate featuring piezoelectric actuators. *Journal of Sound and Vibration* 294: 421–429.

Den Hamer A, Angelis GZ and Roozen N (2005) Broad-band active vibration suppression using PPF focused on industrial application. *IEEE/ASME Transactions on Mechatronics* 10: 146–153.

Dozio L and Ghiringhelli GL (2008) Experiments on active vibration and noise reduction of a panel using predictive techniques. *Structural Control and Health Monitoring* 15: 1–19.

Elliott S (1994) Active control of structure-borne noise. *Journal of Sound and Vibration* 177: 651–673.

Engels WP, Baumann ON, Elliott SJ, et al. (2006) Centralized and decentralized control of structural vibration and sound radiation. *The Journal of the Acoustical Society of America* 119: 1487.

Fahy FJ and Gardonio P (2007) *Sound and Structural Vibration: Radiation, Transmission and Response*. London: Academic Press.

Fanson J and Caughey TK (1990) Positive position feedback control for large space structures. *AIAA Journal* 28: 717–724.

Friswell MI and Inman DJ (1999) The relationship between positive position feedback and output feedback controllers. *Smart Materials and Structures* 8: 285.

Fuller CR, Elliott S and Nelson PA (1996) *Active Control of Vibration*. London: Academic Press.

Gardonio P (2002) Review of active techniques for aerospace vibro-acoustic control. *Journal of Aircraft* 39: 206–214.

Gardonio P, Bianchi E and Elliott S (2004a) Smart panel with multiple decentralized units for the control of sound transmission. Part I: theoretical predictions. *Journal of Sound and Vibration* 274: 163–192.

Gardonio P, Bianchi E and Elliott S (2004b) Smart panel with multiple decentralized units for the control of sound transmission. Part II: design of the decentralized control units. *Journal of Sound and Vibration* 274: 193–213.

Gardonio P, Bianchi E and Elliott S (2004c) Smart panel with multiple decentralized units for the control of sound transmission. Part III: control system implementation. *Journal of Sound and Vibration* 274: 215–232.

Gatti G, Brennan MJ and Gardonio P (2007) Active damping of a beam using a physically collocated accelerometer and piezoelectric patch actuator. *Journal of Sound and Vibration* 303: 798–813.

Gibbs GP, Clark RL, Cox DE, et al. (2000) Radiation modal expansion: application to active structural acoustic control. *The Journal of the Acoustical Society of America* 107: 332–339.

Grewal A, Zimcik D, Hurtubise L, et al. (2000) Active cabin noise and vibration control for turboprop aircraft using multiple piezoelectric actuators. *Journal of Intelligent Material Systems and Structures* 11: 438–447.

Hansen CH (2003) Does active noise control have a future? In: *The Eighth Western Pacific Acoustics Conference*.

Huang NE, Shen Z, Long SR, et al. (1998) The empirical mode decomposition and the Hilbert spectrum for nonlinear and non-stationary time series analysis. In *Proceedings of the Royal Society of London. Series A: Mathematical, Physical and Engineering Sciences* 454: 903–995.

Jemai B, Ichchou M and Jezequel L (2002) Double panel partition (AVNC) by means of optimized piezoceramic structural boundary control. *Journal of Vibration and Control* 8: 595–617.

Ji H, Qiu J, Zhu K, et al. (2009) An improved system of active noise isolation using a self-sensing actuator and neural network. *Journal of Vibration and Control* 15: 1853–1873.

Johnson M and Elliott S (1995) Active control of sound radiation using volume velocity cancellation. *The Journal of the Acoustical Society of America* 98: 2174–2186.

Meirovitch L (1990) *Dynamics and Control of Structures*. New York: John Wiley & Sons.

Meyer Y, Collet M and Delobelle P (2007) Primal–dual optimization process of IFF–DVF active damping strategies. Applications to the beams. *Structural Control and Health Monitoring* 14: 660–680.

Ohayon R and Soize C (1998) *Structural Acoustics and Vibration: Mechanical Models, Variational Formulations and Discretization*. London: Academic Press.

Preumont A (2011) *Vibration Control of Active Structures: An Introduction*. Berlin: Springer.

Rew K-H, Han J-H and Lee I (2002) Multi-modal vibration control using adaptive positive position feedback. *Journal of Intelligent Material Systems and Structures* 13: 13–22.

St Pierre Jr RL, Koopmann G and Chen W (1998) Volume velocity control of sound transmission through composite panels. *Journal of Sound and Vibration* 210: 441–460.

Strassberger M and Waller H (2000) Active noise reduction by structural control using piezo-electric actuators. *Mechatronics* 10: 851–868.

Vipperman JS and Clark RL (1999) Implications of using colocated strain-based transducers for output active structural acoustic control. *The Journal of the Acoustical Society of America* 106: 1392.

Wallace C (1972) Radiation resistance of a rectangular panel. *The Journal of the Acoustical Society of America* 51: 946.

Wang Y and Inman DJ (2011) Comparison of control laws for vibration suppression based on energy consumption. *Journal of Intelligent Material Systems and Structures* 22: 795–809.

Yang JN, Lei Y, Pan S, et al. (2003a) System identification of linear structures based on Hilbert–Huang spectral analysis. Part 1: normal modes. *Earthquake Engineering & Structural Dynamics* 32: 1443–1467.

Yang JN, Lei Y, Pan S, et al. (2003b) System identification of linear structures based on Hilbert–Huang spectral analysis. Part 2: complex modes. *Earthquake Engineering & Structural Dynamics* 32: 1533–1554.

Yuan M, Ji H, Qiu J, et al. (2012) Active control of sound transmission through a stiffened panel using a hybrid control strategy. *Journal of Intelligent Material Systems and Structures* 23: 791–803.